

Interface Tweaking of Perovskite Solar Cells with Carbon Nitride-based 2D Materials

Naveen Harindu Hemasiri¹, Muhammad Ashraf², Samrana Kazim^{1,4}, Robert Graf³,
Rüdiger Berger³, Nisar Ullah², Muhammad Nawaz Tahir^{2,5}, and Shahzada Ahmad^{1,4*}*

¹*BCMaterials, Basque Center for Materials, Applications, and Nanostructures, Bld. Martina Casiano, UPV/EHU Science Park, Barrio Sarriena s/n, 48940 Leioa, Spain
Tel: +34 946128811, Email:shahzada.ahmad@bcmaterials.net*

²*Department of Chemistry, King Fahd University of Petroleum and Minerals, Dhahran 31261, Saudi Arabia*

³*Max Planck Institute for Polymer Research, Ackermannweg 10, Mainz, 55128 Germany*

⁴*IKERBASQUE, Basque Foundation for Science, Bilbao, 48009, Spain*

⁵*Interdisciplinary Research Center for Hydrogen and Energy Storage, King Fahd University of Petroleum and Minerals, Dhahran 31261, Saudi Arabia*

Abstract:

Two-dimensional van der Waals layered materials display strong Coulomb interactions, which in turn give rise to large exciton binding energies. Tuning the interface is the basis of devices including optoelectrical, and their delineation is of paramount importance. The developed 2D-carbon nitrides, display graphene-like atomic structures, and the variation in synthetic protocols impact their properties. Engineering the interface with carbon nitride at hole transport layers and perovskite, can eliminate defective charge build-up and suppress the charge carrier recombination rate to induce accelerated photo-induced charge transfer. The fabricated solar cells with L-C₃N₄ or g-C₃N₄ interface layers gave an improved performance with boosted open-circuit voltage and fill factor. Our interface layers avoid the direct contact of NiO_x with perovskite, overcoming the possible instability of the active layer via iodide oxidation and deprotonation of cationic amines. The carbon nitride-based 2D materials will serve as an effective interfacial layer for long-term reliability in photovoltaics.

Keywords: carbon nitrides, interface engineering, perovskite solar cells, charge transfer dynamics, charge recombination

Introduction

Lead halide based perovskite solar cells (PSCs) have revolutionized the field of emerging photovoltaics and shown rapid progress since its first report in 2009 with power conversion efficiency (PCE) of 3.8% to a certified 25.7% in 2021.¹ In most of the cases the reported highly-efficient PSCs are based on regular architecture (*n-i-p*), in which high-temperature sintered mesoporous TiO₂ is a prerequisite. In contrast, planar inverted (*p-i-n*) architect can be adapted to low-temperature fabrication techniques with potentially high manufacturing processability, giving rise to intense research interest for the flexible substrate; however, PCE trails behind the *n-i-p* devices.^{2,3} One reason is that organic semiconductors compromise stability under operational conditions and lead to low reproducibility. Such barriers impede PSCs rapid advancement and industrialization.

In this context, the interfaces at the perovskite and charge transport layers (CTLs) are critical to controlling the electronic properties through non-radiative recombination, charge/ion accumulation, and charge transport behavior.⁴ Such merits not only determine the efficiency of photo-induced charge collection but also impact the hysteresis in the current (*J*) -voltage (*V*) curves.^{5,6} Moreover, the unfavorable band alignment and interfacial defects at perovskite/CTL interfaces under operational conditions create charge build-up at the interfaces, leading to trap charges which drive degradation and yield a lower open-circuit voltage (*V_{OC}*) in the PSC.⁷ Interface engineering is a straightforward but effective methodology to align the energy band-level at interfaces, to influence the perovskite crystallization and microstructure, defect passivation, and to control ion migration.^{5,8-10} Further, interface engineering overcomes the degradation of perovskite through moisture infiltration, boosting the long-term reliability of PSCs. Organic materials are reported to passivate specific defects of perovskite bulk while improving the quality of the interfacial coupling and eventually enhancing the PV performance.^{2,11-14} In most cases, however, the used organic materials are hygroscopic and can accelerate the degradation mechanism of the perovskite.^{14,15} A rational choice of interfacial materials can influence the electrical, physical, and chemical compatibility of each layer.

Recently, two-dimensional (2D) materials are being explored as interlayers in PSCs, owing to their ease of electronic structure tailoring through functionalization and synthesis route.¹⁶⁻¹⁹ Metal-free carbon nitride (CN) are nontoxic, earth-abundant, polymeric 2D type crystalline semiconductor materials, which display continuous porosity and high surface free energy along with appealing optoelectronic properties.²⁰⁻²² Graphitic carbon nitride (g-C₃N₄) is regarded as

the most studied and highly stable architecture among the five phases of C_3N_4 , composed of tri-s-triazine (s-heptazine), rich in amino ($-NH_2$) and nitrogen, establishing the π -conjugated electronic structure.^{21,22} It displays a moderate bandgap of 2.7 eV with conduction (E_{CB}) and valence (E_{VB}) band edge positions of -1.1 and +1.6 eV, respectively, attributing to the continuous repetition of the heptazine motif.²² The chemical structure of 2D-carbon nitride can be altered by the addition of extra nitrogen-rich moieties, resulting in an extended π -conjugated system of heptazine motif, which leads to a robust and band edge-tuned CN framework.²² g- C_3N_4 has been reported as an additive in perovskite to control the nucleation process thus enhancing the grains and microstructure quality of the perovskite, and measured lower defect density.^{21,23-25} This strategy was further extended and g- C_3N_4 was also noted to enhance the charge transfer dynamics and this mitigates the charge recombination via heterogeneously concentrated carbon nitride additives around perovskite grain boundaries.²⁶ The functionalization of chemically modified CN materials in PSCs boosted the PV performances, through the control of the undesirable charge dynamics at perovskite/CTL interfaces^{20,27}. The use of NiO_x as CTL creates a direct connection to perovskites and prompts iodide oxidation and deprotonate cationic amines (MA^+) which compromises stability.

Here, we have synthesized two graphitic carbon nitride 2D-polymeric materials by solid-state (g- C_3N_4) and solvothermal (L- C_3N_4) synthesis and probed their potential as an interface layer with inorganic hole selective layers in inverted planar triple-cation based PSCs. We investigated their interaction with $[Cs_{0.1}(FA_{0.9}MA_{0.1})_{0.9}Pb(I_{0.9}Br_{0.1})_3]$ at the interface of the layers, and deduced coordination of FA-amine and MA-ammonia groups provides a favorable interaction at the interface between C_3N_4 and perovskite. The enhanced photo-induced charge transfer dynamics and attenuated charge recombination behavior upon 2D-carbon nitrides led to improved PV performances in the PSCs. Subsequently, the low bandgap L- C_3N_4 -modified interlayer-based PSCs gave 19.33%, whereas with high bandgap g- C_3N_4 delivered a PCE of 18.58%, surpassing the control PSCs performance and reliability. A notable value with the use of NiO_x as hole selective layers and suppressed redox reaction at NiO_x /perovskite interface.

Results and discussion

The 2D graphitic-carbon nitride framework is composed of tri-s-triazine connected through planar tertiary amines (Figure 1a), which display two different colors depending on the synthesis method; i.e, solid-state synthesis (g- C_3N_4) is milky yellowish and solvothermal (L-

C₃N₄) is orange in color. The powder X-ray diffraction (XRD) pattern shows two distinct reflections at 2θ values of 27.3° and 12.8° corresponding to the (002) and (100) crystalline planes (Figure 2b) for g-C₃N₄. The strongest (002) reflection with ~ 0.33 nm interplanar d spacing is characteristic of the stacking of the conjugated aromatic system, while the low intense reflection is related to the (100) plane (~ 0.69 nm d spacing) that is correlated to in-planar structural tri-*s*-triazine morphology of g-C₃N₄.^{23,28} The g-C₃N₄ is synthesized at 550°C using solid-state synthesis method where the stacking of 2D-layers is expected to be highly regular (thermodynamic control) than that of L-C₃N₄ which was synthesized at 140°C in solution (kinetic control). However, the reflection indexed to the in-plane structural packing of heptazine units is absent in the case of L-C₃N₄, attributing to the possible distortion in the carbon nitride framework.²¹ We registered the variation in the functional groups and the physical state of the materials by Fourier transform infrared (FTIR) spectroscopy (Figure 1c). A series of IR bands are observed corresponding to C-N stretching of tri-*s*-triazine aromatic nucleus from 1700 to 1000 cm^{-1} in both materials.^{29,30} The combinational symmetric and asymmetric N-H stretches of terminal amino groups induce intense broadband at 2900 - 3500 cm^{-1} in L-C₃N₄.^{21,30} A significantly weak characteristic N-H band arises in g-C₃N₄ owing to the residual $-\text{NH}_2$ present in the carbon nitride framework. The peak observed at around 800 cm^{-1} is assigned to the bending vibration of triazine rings, and is prominent in the case of g-C₃N₄.^{21,29} A subsidiary peak is noted around 2200 cm^{-1} , suggesting the presence of a negligible amount of cyano groups ($\text{C}\equiv\text{N}$), that is favorable for the continuous formation of CN network.³¹⁻³³

Raman spectra represent characteristic peaks at 530 , 750 , and 1025 cm^{-1} core positions related to the breathing mode of the in-plane heptazine rings available in both g-C₃N₄ and L-C₃N₄.³⁰ Further, there are two fingerprint bands at 1320 and 1596 cm^{-1} owing to the disordered D band and graphitic G band, respectively. The broad hump $\sim 1000 - 1800\text{ cm}^{-1}$ observed in both materials can be attributed to the bending of residual $-\text{NH}_2$ and multilayer stacking of carbon nitride layers.²⁹ We recorded the UV-Vis diffuse reflectance spectra (DRS) and g-C₃N₄ shows two absorption peaks at around 280 and 375 nm relevant to $\pi-\pi^*$ transition in the conjugated polymeric network and $n-\pi^*$ transition between nonbonding orbitals of nitrogen and aromatic ring, respectively (Figure 1e).³⁴ Notably, L-C₃N₄ shows a strong absorption shoulder with a red-shifted absorption edge at $\sim 650\text{ nm}$ compared to g-C₃N₄ (absorption edge at $\sim 575\text{ nm}$). This resulted in an upshifted valance band together with $\pi-\pi^*$ transition at low energy and thus the extended absorption in the visible range, exhibiting the orange color of L-C₃N₄.²¹ From the

UV-Vis DRS along with the Kubelka-Munk relationship (Figure 1f), we deduced a reduced optical bandgap from 2.78 eV to 2.29 eV for L-C₃N₄ as compared to g-C₃N₄ in their bulk form, which can be correlated to the J-type aggregation of inter-planar tri-s-triazine rings.³³ Moreover, we calculated the optical band gap of the exfoliated C₃N₄ in iso-propanol/ethanol solution using UV-Vis together with the Tauc plot (Figure S1), and the optical bandgap was calculated to be 3.3 and 2.5 eV for g-C₃N₄ and L-C₃N₄, respectively.

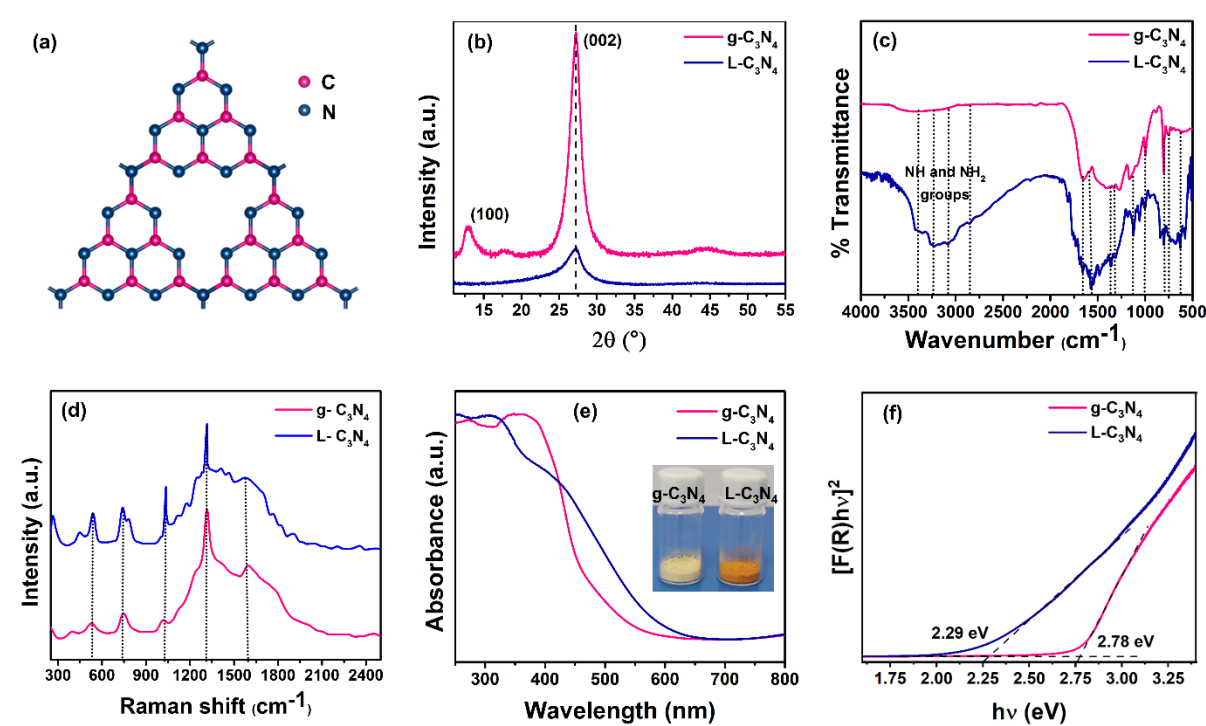


Figure 1. (a) Chemical structure of Tri-s-triazine-based graphitic-C₃N₄, (b) XRD pattern, (c) FTIR spectra, (d) Raman spectra, (e), DR-UV-Vis spectra and inset represents the obtained powders of g-C₃N₄ and L-C₃N₄ and (f) $[F(R)hv]^2$ vs. $h\nu$ plot for g-C₃N₄ and L-C₃N₄.

We performed scanning electron microscopy (SEM) and transmission electron microscopy (TEM) studies of synthesized and exfoliated C₃N₄ materials (Figure 2 and Figure S2). The bulk g-C₃N₄ reveals a highly porous, heterogeneously distributed, and agglomerated structure (Figure 2a) while L-C₃N₄ shows an anisotropic wires-type microstructure (Figure 2b). In the TEM image, the liquid phase assisted (LPA) exfoliated 2D g-C₃N₄ shows the irregular layered structure (Figure S2), consisting of light and dark areas, attributing to the thin nanosheets and overlap or multilayer nanosheets, respectively. Moreover, L-C₃N₄ maintains its random arrangement of anisotropic nanostructure even after the exfoliation (Figure S2b).

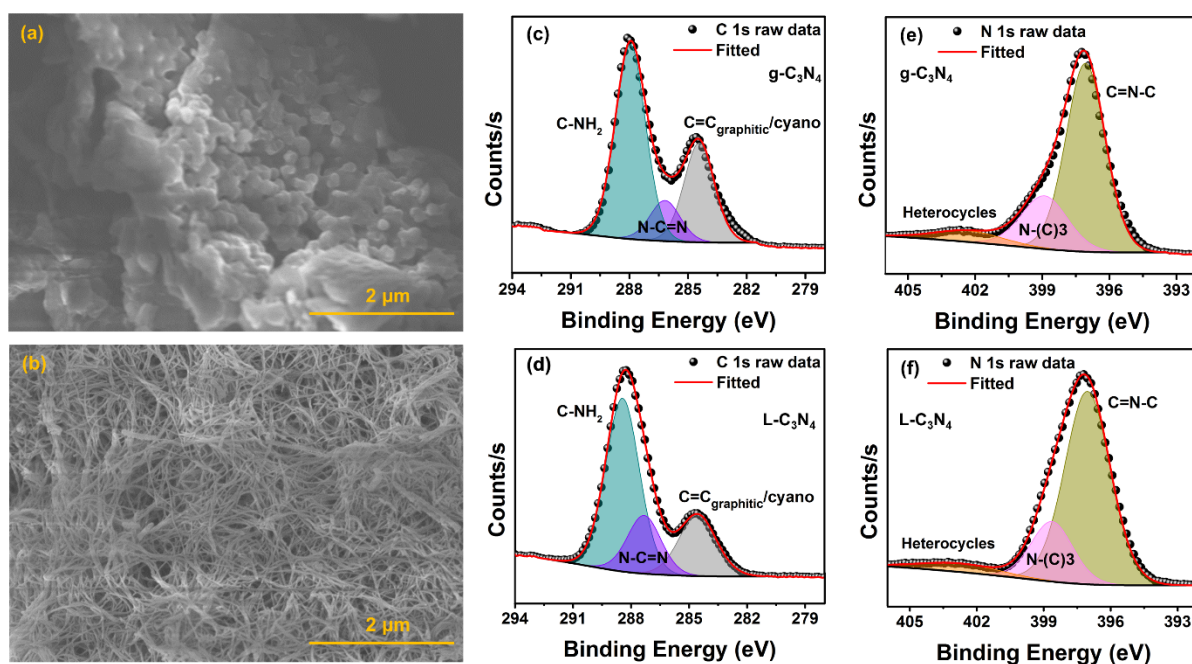


Figure 2. Scanning electron microscopy (SEM) of (a) g-C₃N₄ and (b) L-C₃N₄. High-resolution X-ray photoelectron spectroscopy (XPS) of C1s of (c) g-C₃N₄ and (d) L-C₃N₄, N1s of (e) g-C₃N₄ and (f) L-C₃N₄.

We analyzed the chemical state and composition of the CN materials using X-ray photoelectron spectroscopy (XPS) (Figure 2 c-f and Figure S3). The high-resolution C1s XPS spectrum of g-C₃N₄ (Figure 2e) shows three peak components, which can be assigned to sp² C in aromatic structure (N-C=N) at 286.18 eV, sp² aromatic C attached to NH₂ group at 287.95 eV, and sp³ C-C at 284.43 eV.³² The sp³ carbon peak stems from graphitic or/and cyano group carbon in the C₃N₄ network.^{30,31} Aforementioned three peaks originated at 287.33, 288.44, and 284.56 eV, respectively, in the case of L-C₃N₄. The core level N1s of the g-C₃N₄ show three peaks after deconvolution where the predominant peak at ca. 397.07 eV is assigned to sp² N percent in triazine rings as C=N-C, while the medium peak at 398.9 eV corresponding to bridging N atoms in N-(C)3.²⁷ The positive charge localization or charging effects of heterocycles can further lead to the appearance of a minor peak at around 402.29 eV.^{20,31,32} The above peaks at 397.04, 398.63, and 402.75 eV, respectively were observed in the case of L-C₃N₄. Additionally, two peak components were recognized in Cl2p from L-C₃N₄ at a binding energy of 198.69 and 195.29 eV, attributing to Cl2p_{1/2} and Cl2p_{3/2}, respectively (Figure S4).

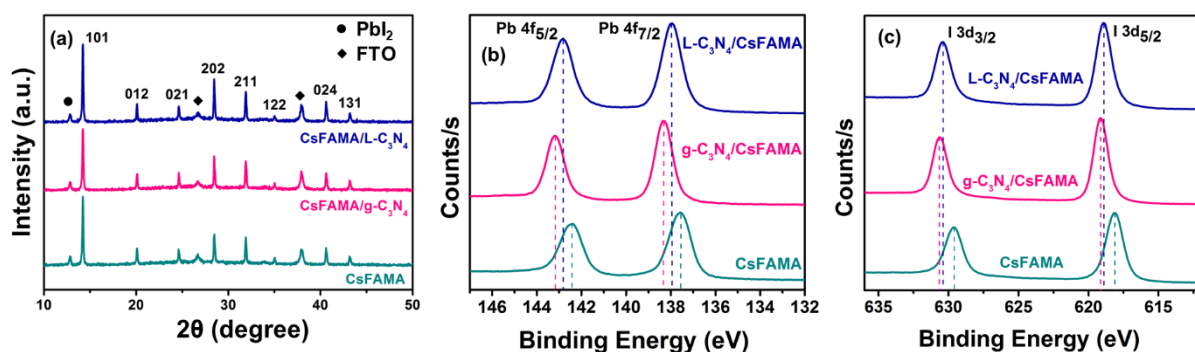


Figure 3. XRD patterns of CsFAMA deposited on NiO_x, g-C₃N₄/NiO_x, and L-C₃N₄/NiO_x. High-resolution XPS of (a) Pb4f and (b) I3d detected from CsFAMA, CsFAMA/g-C₃N₄, and CsFAMA/L-C₃N₄ [here CsFAMA denotes Cs_{0.1}(FA_{0.9}MA_{0.1})_{0.9}Pb(I_{0.9}Br_{0.1})₃].

We studied the film-forming ability of C₃N₄ and the surface coverage of perovskite on C₃N₄ using microscopic studies (Figures S5 and S6). We noted uniform layers of L-C₃N₄ over NiO_x as compared to g-C₃N₄ on NiO_x. SEM images of perovskite (triple cation perovskite is termed as CsFAMA) layers directly deposited on g-C₃N₄ and L-C₃N₄ show a slightly enhanced grain size as compared to of NiO_x film. The corresponding histogram of the grain size distribution is shown in Figure S6a'-c' with the average grain size (length) of 202.4, 208, and 209.1 nm for the perovskite grown on NiO_x, g-C₃N₄/NiO_x, and L-C₃N₄/NiO_x, respectively. Moreover, a compact microstructure was noted upon g-C₃N₄ and L-C₃N₄ placement, suggesting its impact on perovskite crystallization. The powder XRD (Figure 3a) patterns of the perovskite deposited on CN under layer display a notably increased ratio of the (101) plane to (012), (021), (211), and (122) crystal planes without a shift in the reflection, attributing faster growth and preferential orientation of (101) grains with the absence of influence from the down layer. The absorption of the CsFAMA layer is unchanged by the CN under layer as depicted in UV-Vis absorption spectra (Figure S7). We further performed XPS measurements to unravel the potential interactions of the underlayer C₃N₄ materials with perovskite. For this, CsFAMA powder was collected after spin-coated onto the g-C₃N₄ and L-C₃N₄ separately. Compared with control CsFAMA, g-C₃N₄ and L-C₃N₄ incorporated CsFAMA showed core-level peaks of Pb 4f and I 3d (Figure 3b, c) that were shifted towards higher binding energies. This phenomenon indicates that the CN materials impact the chemical environment of the [PbI₆]⁴⁻ octahedron.^{11,35,36} Additionally, the core-level peaks of Cs 3d, N1s, and C1s are shown (Figure S8 and Figure S9) and the individual peak positions were tabulated (Table S1). A visible peak was observed at around 800 cm⁻¹ from the FTIR of the C₃N₄-modified CsFAMA, which can

be assigned to the bending vibration of triazine rings, showing evidence of the existence of C_3N_4 materials (Figure S10).

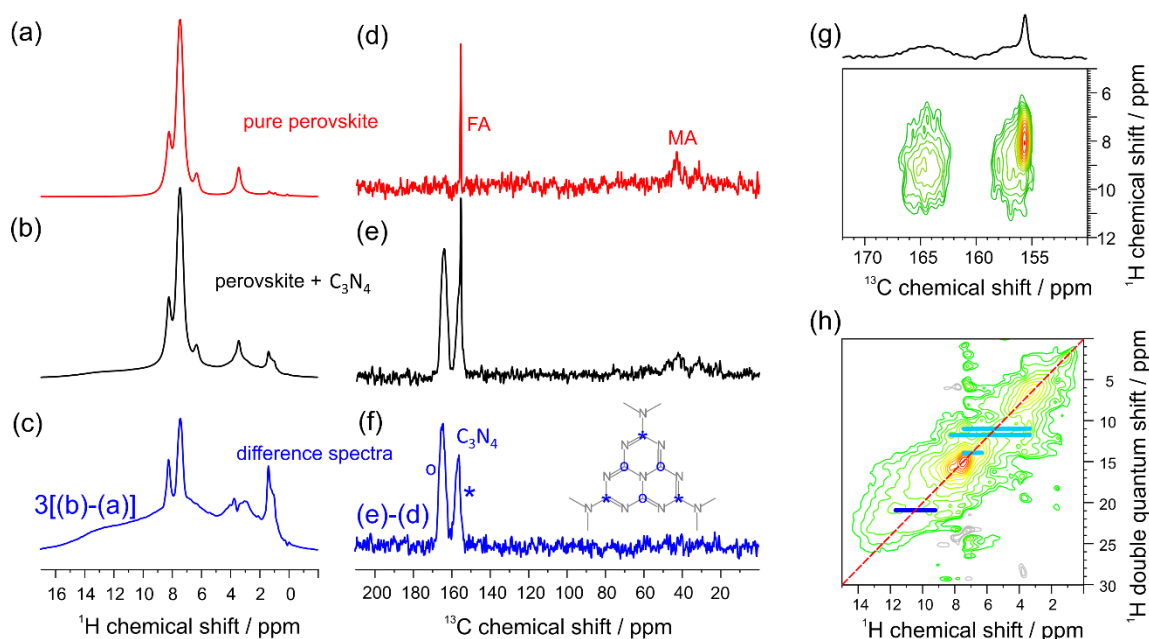


Figure 4: Solid-state NMR results of CsFAMA perovskite samples with and without C_3N_4 addition: (a,b) 1H MAS and (d,e) ^{13}C CP-MAS NMR spectrum of CsFAMA perovskite, pure and blended with C_3N_4 material, respectively, and the resulting 1H (c) and ^{13}C (f) difference spectra. (g) 1H - ^{13}C CP-MAS correlation spectrum of the perovskite + C_3N_4 material acquired with 5ms CP-contact and (h) the 1H DQ correlation spectrum of the same material with 1 rotor period BABA-xy16 DQ excitation at 25 kHz MAS.

We undertook solid-state NMR studies to deduce possible changes in the atomistic environment of the MA and FA cations at the interface of the C_3N_4 and perovskite. From NMR studies by Kubicki et al., it is known that FA and MA cations of the mixed-perovskites exhibit at ambient conditions fast in-place reorientation dynamics with 10 ps and 100 ps correlation time, respectively, with only minor variations depending on the FA/MA mixing ratio.³⁷ These fast molecular motions facilitate the acquisition of highly resolved 1H MAS spectra of CsFAMA at moderate MAS spinning frequencies of 25 kHz (Figure 4a). Upon mixing the perovskite with C_3N_4 , broad background signals appear between 3 – 14 ppm together with residual solvent signals around 1 ppm (Figure 4b). The broadened FA and MA signals can be visibly deduced when the signals of pure bulk perovskite, i.e. signals of perovskite sites that are not in direct contact with the C_3N_4 surface and therefore are unaffected by the blending, are subtracted from the spectrum. The deduced spectrum (Figure 4c) shows residual FA signals,

indicating that the MA cations have stronger coordination with the C_3N_4 . In the NMR spectrum, the methyl signal of the coordinating MA ions stays at the same chemical shift as in the bulk perovskite, whereas the amine and ammonia signals of FA and MA shift to higher ppm values. This shift towards higher ppm values indicates an electronic deshielding of the 1H sites, which is often indicative of hydrogen bonding. Here, positively charged hydrogen sites may coordinate with unbound nitrogen electron pairs at the edges of the triangular inner voids of the two-dimensional C_3N_4 . This coordination stops the almost isotropic local dynamics of the cations at the interface of the perovskite and leads to broad 1H MAS signals with significantly shorter T_1 relaxation time ($\sim 3s$). In the ^{13}C CP-MAS NMR spectra of perovskite samples with and without C_3N_4 (Figure 4e, and 4d respectively) acquired at ambient conditions, the FA-CH site is noted as the sharp signal at 155 ppm, similar to low-temperature measurements.³⁷ The MA-CH₃ signals around 30 ppm, however, show a significantly bigger splitting, and a substantial broadening is observed in our spectra compared to the published low-temperature CP-MAS spectra which may originate from additional processing steps. By subtracting the CP-MAS NMR spectrum of the pure perovskite (Figure 4d) from the spectrum of the perovskite- C_3N_4 (Figure 4e) the ^{13}C CP-MAS spectrum of the C_3N_4 (Figure 4f) with two broad signals at 165 ppm and 157 ppm can be obtained. The two signals, which have equal intensity for CP-MAS acquisition with longer CP contact times, are assigned to the two chemically inequivalent carbon sites in the C_3N_4 structure. The 1H - ^{13}C CP-MAS correlation spectrum (Figure 4g) demonstrates that the ^{13}C nuclei of the C_3N_4 are primarily polarized via immobilized hydrogen nuclei bound to a nitrogen atom. Polarization transfer from strongly hydrogen-bonded protons around 12 ppm as well as from MA-methyl or FA-CH protons to the C_3N_4 , ^{13}C sites is not observed. The 1H double-quantum (DQ) correlation spectrum (Figure 4h), recorded with 40 μs DQ excitation time, confirms the homogeneous distribution of MA cations in the material, e.g. the intermolecular correlation between MA ammonia sites and FA amine sites compared to intramolecular ammonia correlations (Figure h), light blue correlation.³⁸ The correlation highlighted in dark blue, however, indicates the spatial proximity between NH-protons strongly hydrogen-bonded to the C_3N_4 and their neighboring hydrogen sites within the FA-amine and MA-ammonia groups. Simple MM2-MD simulations of the behavior of FA and MA molecules at the C_3N_4 surface support this behavior and suggest significantly stronger coordination of the ammonia groups due to competing pi-electron interaction in the case of FA. The deduced coordination of FA-amine and MA-ammonia groups suggests an attractive interaction at the interface between C_3N_4 and perovskite, which stems from the stabilization of the FA and MA cations at the interface as a passivation layer for the perovskite.

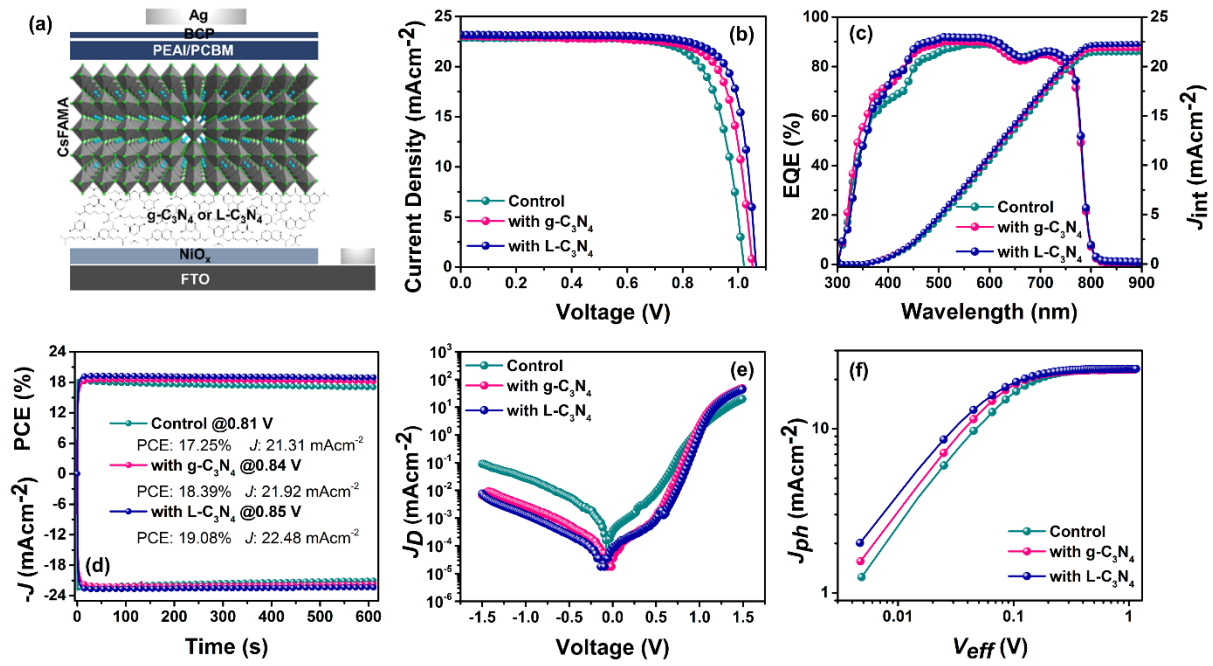


Figure 5. (a) Device configuration, (b) J - V curve of the champion devices without and with $g\text{-C}_3\text{N}_4$ or $\text{L-C}_3\text{N}_4$ interface layer measured in reverse scan under simulated AM 1.5G illumination, (c) IPCE and integrated current density of the corresponding devices, (d) steady-state power output of PSCs. (e) dark J - V curves and (f) photo-generated current density vs. effective voltage of PSCs.

We fabricated the PSCs based on inverted architecture using $g\text{-C}_3\text{N}_4$ and $\text{L-C}_3\text{N}_4$ as interface layers in-between NiO_x and perovskite absorber layers (Figure 5a). We employed triple-cation perovskite as the photoactive layer (thickness of ~ 420 nm, Figure S11) deposited on NiO_x or interface layer (C_3N_4) by an antisolvent-assisted spin-coating technique. The concentration of the interfacial layer was optimized to 1.25 mg/ml (Figure S12, Table S2). The estimated thickness of the C_3N_4 layer is ~ 12 nm, as deduced from atomic force microscopy (AFM) experiments (Figure S13). Detailed information on the fabrication process is provided in the Experiment section. The current density-voltage (J - V) curves of the PSCs were registered under standard solar illumination (AM 1.5G, 100mWcm^{-2}) (Figure 5b) and summarized in Table 1.

Devices gave 16.85, 17.67, and 18.21% performances from control, $g\text{-C}_3\text{N}_4$ -based, and $\text{L-C}_3\text{N}_4$ -based, respectively. We further deposited PEAI at the perovskites/ ETM layer and the maximum PCE of 17.48% with an open-circuit voltage (V_{OC}) of 1020.93 mV, a short-circuit current density (J_{SC}) of 22.86 mAcm^{-2} , and a fill-factor (FF) of 74.88% under reverse scan was

measured for the control device. The L-C₃N₄ interface layer effectively yielded an improved PCE of 19.33% with a significant enhancement in V_{OC} (1064.37 mV) and FF (78.35). In particular, the PSCs with g-C₃N₄ interlayer also showed us a visible development in PCE, and an optimized PSC provided 18.58% PCE with V_{OC} of 1051.50 mV, J_{SC} of 23.05 mA, and FF of 76.64%.

Table 1. Summary of the PSC performances using with and without different C₃N₄ interlayers. The device statistics are from 12 devices, and only 1 device/substrate.

Devices	Scan direction	V_{OC} (mV)	J_{SC} (mAcm ⁻²)	FF (%)	PCE (%)
NiO _x	Reverse	1020.93	22.86	74.88	17.48
	Forward	1021.90	22.85	73.90	17.26
	Average	1007.8±8.7	22.77±0.14	72.69±1.18	16.68±0.43
NiO _x /g-C ₃ N ₄	Reverse	1051.50	23.05	76.64	18.58
	Forward	1053.12	23.03	75.78	18.38
	Average	1032.36±15.8	22.98±0.07	74.76±0.96	17.74±0.48
NiO _x /L-C ₃ N ₄	Reverse	1064.37	23.18	78.35	19.33
	Forward	1063.97	23.11	77.97	19.11
	Average	1049.77±9.2	23.05±0.12	75.60±1.33	18.30±0.52

The voltage deficit was minimized and the significant reduction in V_{OC} loss with the L-C₃N₄-based interfacial layer can be attributed to the constructively annihilated recombination losses at NiO_x/perovskite interface. Notably, a high fill factor is noted with C₃N₄ interfacial layer in PSCs due to improved charge dynamics arising from the improved crystallization in the perovskite active layer and better charge collection to NiO_x as HTL at the interface developed here with minimum parasitic losses from shunt (R_{sh}) and series (R_s) resistances (Table S3).^{12,39} The R_{sh} and R_s were detected from the slop of the J - V curves near J_{SC} and V_{OC} , respectively. High R_{sh} in combination with low R_s detected represents the suppressed nonradiative charge recombination and interfacial charge losses in the PSCs with modified interfaces.^{12,16,40} We calculated the hysteresis index using the equation; $HI = [J_{RS}(0.8V_{OC}) - J_{FS}(0.8V_{OC})] / J_{RS}(0.8V_{OC})$, where $J_{RS}(0.8V_{OC})$ and $J_{FS}(0.8V_{OC})$ denote the J_{SC} at 80% of V_{OC} from reverse and forward scan, respectively. Remarkably, both C₃N₄-based PSCs showed negligible hysteresis index in the J - V scans of reverse and forward bias (Table S3 and Figure S14). The integrated

photocurrent densities collected from the external quantum efficiency (EQE) spectra (Figure 5c) were 21.44, 21.86, and 22.28 mAcm⁻² for NiO_x, NiO_x/g-C₃N₄, and NiO_x/L-C₃N₄, respectively, agree with the *J-V* curves. The enhancement of EQE observed in the region of 400-500 nm in the devices with L-C₃N₄ and g-C₃N₄ could be attributed to the improved grain size of perovskite, owing to the higher absorption due to a higher absorption coefficient of the perovskite at shorter wavelength⁴¹. The steady-state power output (SPO, Figure 5d) stabilized at 19.08% of PCE (with 22.48 mAcm⁻² at 0.85V) upon L-C₃N₄ whereas, for g-C₃N₄, those were at approximately 18.39% and 21.92 mAcm⁻² at 0.84V under ambient conditions (~40-60 % RH at 28 °C). Figure S15 a-d shows the statistical distribution of PV parameters of the devices (54 devices in each category) from different batches, which indicates the excellent reproducibility of the PSCs with C₃N₄-based interface engineering.

To quantify the improvement in FF, we measured resistance losses and leakage current behavior from the *J-V* profile under dark conditions (Figure 5e). The reverse saturation currents of the L-C₃N₄ and g-C₃N₄-PSCs are reduced as compared to the control PSC. The ideality factor n_{id} was quantized from the Shockley liner part of the semi-logarithmic dark *J-V* profile based on the; $J_D = J_0 \left[\exp\left(\frac{qV}{n_{id}K_B T}\right) - 1 \right]$, where J_D is the dark current density, J_0 is the saturation current density, q is the electron charge, V is the applied bias, K_B is the Boltzmann constant, and T is the temperature.^{16,42} The shifting of the dark current (J_D) minimum point and the exponential area in PSCs are significantly influenced by changes in the electric field, scanning rate, and temperature.^{6,43} Since the external factors such as scanning rate and the temperature were constant during the experiment in each case, the slight shifting of the J_D minimum point upon C₃N₄ interface layers with respect to that of the control device could be attributed to the modification of an internal built-in electric field of the devices. The calculated J_0 and n_{id} for the PSC with L-C₃N₄ were 4.346×10⁻⁸ mAcm⁻² and 2.29, respectively, whereas for the PSC with g-C₃N₄ were 4.918×10⁻⁷ mAcm⁻² and 2.55, respectively, which are significantly lower than that of the control device (2.564×10⁻⁵ mAcm⁻², 3.36). Such low J_0 and n_{id} observed in the PSCs with C₃N₄ interfacial layers indicate a low leakage current density and notably inhibited photo-charge recombination, thus resulting in upgraded FF.⁴² The lowest J_0 and n_{id} detected from the L-C₃N₄-based PSCs further describe the enhanced photo-induced charge transfer dynamics in the PSCs, which is beneficial towards V_{OC} improvement, and subsequently boosts the PCE.

To decipher, the effect of the C₃N₄ network as an interfacial layer on the photo-induced charge transfer dynamics in PSC, charge generation, and dissociation were particularly identified, by following the effective voltage (V_{eff}) dependent photocurrent density (J_{ph}) (Figure 5f). Herein, V_{eff} and J_{ph} are defined by $V_{eff} = V_0 - V_{app}$ and $J_{ph} = J_L - J_D$ respectively, where V_0 is the compensation voltage obtained at $J_{ph} = 0$, V_{app} is the applied bias voltage, J_L is the current density under illumination, and J_D is the current density under dark conditions.^{44,45} The saturation of photocurrent (J_{sat}) for L-C₃N₄ and g-C₃N₄ based PSCs were detected at a relatively low V_{eff} of 0.287 and 0.368 V, respectively, when compared with that of the control device (0.428 V), which we attribute to the constructive charge dissociation and separation in the PSCs upon interface engineering with C₃N₄.⁴⁵ Furthermore, the efficiency of charge dissociation from photogenerated excitons and free charge collection ultimately depends on the maximum exciton generation rate (G_{max}), following $J_{sat} = qLG_{max}$, where L is the perovskite layer thickness.¹⁶ It has been calculated that the G_{max} is slightly higher upon L-C₃N₄, reaching $3.447 \times 10^{21} \text{ S}^{-1}\text{cm}^{-3}$ when compared with g-C₃N₄-based PSC ($3.426 \times 10^{21} \text{ S}^{-1}\text{cm}^{-3}$) and control PSC ($3.398 \times 10^{21} \text{ S}^{-1}\text{cm}^{-3}$). The boosted charge carrier generation and the exciton generation rate further explain the improved EQE upon C₃N₄ interlayers.⁴⁶

Electrochemical impedance spectroscopy (EIS) under dark conditions was carried out to gain insight into photo-induced charge carrier recombination behavior at HTL/perovskite interface in PSCs with interfacial engineering. The resulting Nyquist plot at 0.9 V bias voltage was fitted (Figure S16a) with the equivalent circuit model of $R_s + R_{rec}/\text{CPE}$ (Figure S14b), where R_s is series resistance, R_{rec} is recombination resistance at the perovskite/NiO_x interface, and CPE is a carrier diffusion-based constant phase element. The obtained R_{rec} of the L-C₃N₄-based PSC after fitting the Nyquist plot at 0.9V applied bias features a higher value followed by the g-C₃N₄-based and control PSC (Table S4). Owing to the inverse proportionality, the interfacial charge recombination was remarkably subdued upon the L-C₃N₄ interface layer, followed by the g-C₃N₄ interface layer, and thus significant improvements in V_{OC} in L-C₃N₄ and g-C₃N₄ PSCs, when compared with the control PSC.^{16,47} Furthermore, the trend of R_{rec} is consistent with the trend of R_{sh} detected from the J - V profile.

The influence of different interfacial layers on the charge lifetime (τ) of the PSCs was further identified by bode EIS spectra under the dark condition at 0.9 V applied bias (Figure S17) with the relationship of $\tau = 1/(2\pi f_p)$, where f_p denotes the peak frequency corresponding to the charge-transfer process at the perovskite/NiO_x interface.^{48,49} The charge lifetime of the PSCs

with L-C₃N₄ and g-C₃N₄ were 6.65 and 5.20 μ s, respectively, which are significantly longer than that of the control device (2.49 μ s). The extended charge lifetime upon L-C₃N₄ and g-C₃N₄ can be concluded to the annihilated charge build-up and mitigated charge recombination at the interface, thus resulting in proper charge transfer dynamics towards the upgraded PV performances in PSCs.⁴⁹ Reduced trap-assisted recombination was further identified by measuring the space-charge-limited current–voltage (J – V) curves of the hole-only device with the structure of FTO/NiO_x/C₃N₄(with or without)/perovskite/PTAA/Au. As shown in Figure S18 a-c, the limit voltage of the trap-filled (V_{TFL}) is determined to be 0.317, 0.250, and 0.209 V for the control, g-C₃N₄, and L-C₃N₄ based devices, respectively. The defect density; N_{trap} [which is followed by the equation $N_{trap} = (2\epsilon\epsilon_0 V_{TFL})/(qL^2)$, where, ϵ is the relative permittivity, ϵ_0 is the vacuum permittivity, q is the elementary charge, and L is the perovskite thickness]¹¹ was calculated to be 5.77×10^{15} and 6.89×10^{15} cm⁻³ upon g-C₃N₄ and L-C₃N₄, respectively, those are much lower than that of the control device with 8.72×10^{15} cm⁻³.

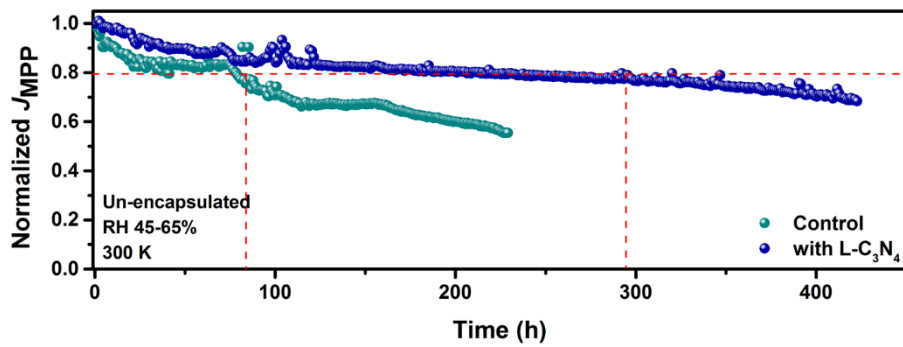


Figure 6. The normalized current density of continuous MPP tracking for unencapsulated PSCs under atmospheric conditions (RH 45-65 %, 300 K).

Despite the excellent intrinsic stability observed in inorganic NiO_x, a possible redox reaction at NiO_x/perovskite initiates and promotes the degradation of the active layer and subsequently the instability of the devices.^{50,51} Dual behavior (proton acceptor and Lewis electron acceptor) of Ni²⁺ in NiO_x is responsible for the oxidizing iodide and deprotonating cationic amines (MA⁺) when in contact with perovskite, resulting in perovskite lattice deformation and producing PbI_{2-x}Br_x based hole extraction barriers at the interface. To unravel the influence of the L-C₃N₄ interface layer to overcome the possible degradation of perovskite and defect pathways from NiO_x, long-term operational stability of the un-encapsulated PSCs with and without the L-C₃N₄ interface layer was investigated through maximum power point tracking under 45-65 % ambient RH conditions. The prolonged stability of the device (Figure 6), by the

placement of the L-C₃N₄ interface layer, was exhibited when compared with the control device. The control device rapidly lost 20% of its initial PCE after 85h of continuous, while the L-C₃N₄ incorporated device exhibited 80% of its initial PCE for almost 300h of continuous operation. Further, we studied the structural stability of the perovskite layer deposited on different buried layers under constant thermal and illumination conditions. Samples were heated at 85 °C for about 110h under daylight and RH 55-75% conditions followed by XRD measurements (Figure S19a-c). In the fresh samples, two major peaks at 14.10° and 28.33° corresponding to (101) and (202) crystal planes, respectively, characteristics of perovskite are identified. After thermal/light exposure, a peak at 12.71° corresponding to the cubic PbI₂ was detected as the predominant peak from the perovskite directly deposited on NiO_x with a 1.12:1 intensity ratio of PbI₂ and (101). Even though, perovskites deposited on g-C₃N₄/NiO_x and L-C₃N₄/NiO_x films also feature a significantly intense PbI₂ peak after the thermal/light exposure, their intensity ratios with (101) plane are 0.86:1 and 0.83:1, respectively. A prominent peak observed from the perovskite/NiO_x after the thermal/light exposure at 11.24° is recognized as the δ -phase of FAPbI₃, which is the major part in the triple-cation perovskite studied in the current work.^{52,53} This peak is marginal upon C₃N₄ interlayers in between the perovskite and NiO_x, suggesting that the structural distortion and degradation of the perovskite is noticeably lower with the presence of g-C₃N₄ and L-C₃N₄ interlayers. Moreover, we probed the absorption features for the aforementioned perovskite films after the thermal/light exposure (Figure S20). After thermal/light stress, the samples showed a decreased absorption, however, this is particularly pronounced in the perovskite/NiO_x sample, which has started to depart from its original dark color. Suggesting, the thermal/light stress impacts the stability of the perovskite when directly deposited on NiO_x. The perovskite deposited on g-C₃N₄/NiO_x and L-C₃N₄/NiO_x, on the other hand, exhibits a minute discoloration and retains the majority of its dark state, pointing towards the suitability of the placed C₃N₄ layers on the stability of the perovskite. To note here these experiments were made on the unencapsulated perovskite films, where the humidity may impact the degradation of perovskite that is assumed to be equal in each film.

Conclusions

To summarize, we demonstrated interface engineering of inverted PSCs using carbon nitride-based 2D materials, in particular g-C₃N₄ and L-C₃N₄. Our work demonstrates the potential of carbon nitride as an interfacial layer to diminish the non-radiative recombination and enhance charge transfer dynamics at HTM/perovskite interface. Through C₃N₄-based engineered

interfaces we achieved an improvement in device performance and reliability as compared to the control architecture, measuring a power conversion efficiency of 19.33%, with complete suppression of the device hysteresis using inorganic HTMs. The solid-state NMR experiments suggest a hydrogen bonding of MA⁺ cations with C₃N₄. We noted that the positively charged hydrogen sites can coordinate with unbound nitrogen electron pairs at the edges of the triangular inner voids of the two-dimensional C₃N₄. The deduced coordination of FA-amine and MA-ammonia groups provides a favorable interaction at the interface between C₃N₄ and perovskite. Furthermore, C₃N₄ may overcome the possible instability of the active layer via iodide oxidation and deprotonating of cationic amines when perovskite is in contact directly with NiO_x, leading to improved long-term operational stability of the devices. Our investigation distinctly illustrates the advancement of 2D-based materials as an interface layer to uplift the reliability of the PSCs, which will pave the way for the industrial endeavor.

Experimental section

Materials: The chemicals for perovskite were purchased from Dyesol except for PbI₂ and CsI₂ which were procured from Tokyo Chemical Industry (TCI) and were employed without further purification. [60]PCBM >99.5 % and Bathocuproine (BCP) were purchased from Solenne BV and TCI, respectively. Nickel (II) nitrate hexahydrate (Ni(NO₃)₂·6H₂O, 99.999 %) and NaOH were obtained from Sigma-Aldrich. Chlorobenzene (CB, 99 %), isopropanol (IPA, 99.9 %), ethanol (EtOH, 99 %), anhydrous dimethyl sulfoxide (DMSO, 99.8 %), and N, N-dimethylformamide (DMF, 99.8 %) were purchased from Acros Organics.

C₃N₄ materials synthesis and solution preparation:

Synthesis of L-C₃N₄: The L-C₃N₄ was synthesized using a solvothermal procedure as reported⁵⁴ with modifications of using acetonitrile as solvent. Briefly, cyanuric chloride (2 mmol) and melamine powder (1 mmol) were mixed in 150 ml in 30 ml of acetonitrile. The mixture was added to a Teflon-lined autoclave with a volume of 100 ml under inert conditions. The mixture was stirred for 10 h at room temperature before it was kept in an electric oven at 140 °C for 12 h. After cooling the contents of the autoclave to room temperature, the suspension was filtered and sequentially washed with acetonitrile, DI water, and ethanol three to four times. The collected samples were dried in an oven overnight at 50 °C.

Synthesis of g-C₃N₄: The graphitic carbon nitride (g-C₃N₄) was prepared by heating 10 g melamine at 550 °C at ramping of 2 °C/minute. The temperature was held at 550 °C for 4 h under inert conditions in the horizontal tube furnace using an alumina crucible. After cooling the furnace to room temperature, the yellowish product was obtained and used.

Preparation of C₃N₄-based solutions: To prepare C₃N₄-based solutions, 5 mg of each material was dissolved in 1 ml of isopropanol/absolute ethanol (70/30, V/V) mixture by sonication for 8 h at 45 °C and rest for 30 min. The upper part of the solution was collected and ultra-centrifuged for 15 min at 2000 rpm. The supernatant was carefully collected and precipitation was discarded. The final concentrations (1, 1.25, and 1.5 mg/ml) were adjusted by adding the mixture of isopropanol/absolute ethanol (70/30, V/V).

Device fabrication: The pre-cleaning process of laser-etched FTO-coated glass substrates (TEC15) was conducted by sequential sonication with Hellmanex II (2 vol.% in deionized water), deionized water, ethanol, acetone, and isopropanol, followed by drying via compressed airflow. The substrates were further treated with UV-ozone for 30 min before use. NiO_x films were formed atop FTO substrates by spin coating at 4000 rpm for 35 s with 2000 rpm/s acceleration, followed by annealing at 150 °C for 30 min (the synthesis of NiO_x was described in our previous work).⁴⁵ The solutions of g-C₃N₄ and L-C₃N₄ with different concentrations were spin-coated on the NiO_x layer and annealed at 60 °C for 5 min to achieve the desired interfacial layer. To avoid moisture absorption, samples were transferred immediately to the argon-filled glovebox under controlled moisture and oxygen conditions (H₂O level: <1 ppm and O₂ level: <10 ppm) and annealed for another 5 min at 60 °C. The triple-cation-perovskite [Cs_{0.1}(FA_{0.9}MA_{0.1})_{0.9}Pb(I_{0.9}Br_{0.1})₃] film was fabricated by a single-step method involving the CB-based antisolvent technique. The perovskite precursor solution was made according to the previous report.¹⁴ The precursor solution was spin-coated in a two-step spin-coating program set at 1000 rpm and 6000 rpm for 10 and 30 s, respectively. During the second spin step, 112 µL of CB was dripped 10 s before the ending of the program followed by annealing at 100 °C for 1 h. For PEA treatment, the PEA solution (20 mg/mL) in IPA was spin-coated onto the perovskite surface at a spin rate of 3000 rpm (2000 rpm/s) for 20 s without further processing. The electron transport layer was fabricated by spin-coating a 15 mg/ml PCBM in CB at room temperature atop the perovskite film at 1000 rpm (500 rpm/s) for 20 s and then the films were annealed for 5 min at 60 °C. A thin layer of BCP (0.5mg/ml in IPA) was deposited atop PCBM by spin-coating at 5000 rpm for 40 s. The solar cell fabrication was finished by

evaporating Ag (100 nm, $<1 \text{ \AA/s}$) in a thermal evaporator under low vacuum conditions (10^{-6} Torr). The control device was fabricated according to the above procedure without the interfacial layer.

Device characterization: Current density–voltage (J – V) curves were measured under air-mass (AM) simulated 1.5G sunlight at 100 mWcm^{-2} (Newport, AAA solar simulator, calibrated using silicon reference cell) and were recorded by applying an external potential bias to the devices. The measurements were done at room temperature under ambient conditions. The generated photocurrent was recorded at a scan rate of 100 mV/s (pre-sweep delay: 10s) with the help of a Keithley 2400 source meter and laser cut 0.09 cm^2 black metal mask as the active area. IPCE measurements were carried out using a 150 W xenon lamp attached to a Bentham PVE300 motorized $1/4 \text{ m}$ monochromator as the light source and the system was calibrated with the standard silicon reference spectrum before the measurements. BioLogic SP-300 impedance analyzer conducted the electrochemical impedance spectroscopy and the data were fitted with EC-Lab software.

Materials and thin film characterization: The absorbance spectra of thin films were performed with a UV–vis spectrophotometer (Varian Cary 50 UV/Vis Spectrophotometer). X-ray diffractograms were recorded using a D8 Advance diffractometer from Bruker (Bragg-Brentano geometry, with an X-ray tube Cu $K\alpha$, $\lambda = 1.5406 \text{ \AA}$). A scan range of 3° – 80° was selected with an acquisition time of 1° per min. A scanning electron microscope (SEM Hitachi S-4800) was used to capture the cross-sectional and top-view microstructure of the samples. X-ray photoelectron spectroscopy (XPS) experiments were carried out on a SPECS system (Berlin, Germany) equipped with Phoibos 150 1D-DLD analyzer with monochromated Al $K\alpha$ radiation (1486.7 eV). The wide scan was performed with the step energy of 1 eV (dwell time, 0.1 s ; pass energy, 80 eV), and a high-resolution detailed analysis of the elements was performed using 0.08 eV step energy (dwell time, 0.1 s ; pass energy, 30 eV) with an electron exit angle of 90° . The spectra were calibrated with C1s as 284.6 eV and analyzed using CasaXPS 2.3.16 software, which models Gauss–Lorentzian contributions.

Sample preparation for solid-state NMR: The solutions of exfoliated g- C_3N_4 and L- C_3N_4 (1.25 mg/mL) in a mixture of isopropanol/absolute ethanol (70/30, V/V) were spin-coated on pre-cleaned glass substrates and annealed at 60°C for 5 min. The triple-cation perovskite precursor in DMF/DMSO (4/1, V/V) was spin-coated to fabricate the perovskite films by a single-step method involving the CB-based antisolvent technique. After the complete crystallization of

perovskite, the samples were cooled down to room temperature, and collected powder samples by scratching the films.

Conflicts of interest

The authors declare no conflict of interest.

Author Contributions

NHH performed the experiments, analyzed the data, and prepared the initial draft, MA synthesized the C_3N_4 materials and made spectroscopic characterization, NU, and MNT supervised his research. SK performed the electro-optical measurements and supervised NHH, RG, RB performed ss-NMR experiments and analysis of the data and hypothesis. SA conceived the idea, & directed the research. All authors commented on the draft.

Acknowledgments

This work received funding from the European Union H2020 Programme under a European Research Council Consolidator grant [MOLEMAT, 726360]. SA and SK thank from INTERACTION (PID2021-129085OB-I00) and ARISE (PID2019-111774RB-I00), from the Spanish Ministry of Science and Innovation. We thank SGIKER, UPV-EHU for the XPS analysis.

References

1. <https://www.nrel.gov/pv/cell-efficiency.html> (accessed: February 2022).
2. X. Li, W. Zhang, X. Guo, C. Lu, J. Wei, J. Fang, *Science*, 375 (2022), 434–437.
3. F. Li, X. Deng, F. Qi, Z. Li, D. Liu, D. Shen, M. Qin, S. Wu, F. Lin, S. Jang, J. Zhang, X. Lu, D. Lei, C. Lee, Z. Zhu, A. –Y. Jen, *J. Am. Chem. Soc.*, 142 (2020), 20134–20142.
4. S. Shao, M. A. Loi, *Adv. Mater. Interfaces*, 7 (2019), 1901469.
5. P. Schulz, D. Cahen, A. Kahn, *Chem. Rev.*, 119 (2019), 3349–3417.

6. W. Tress, N. Marinova, T. Moehl, S. M. Zakeeruddin, M. K. Nazeeruddin, M. Grätzel, *Energy Environ. Sci.*, 8 (2015), 995–1004.
7. B. Chen, M. Yang, S. Priya, K. Zhu, *J. Phys. Chem. Lett.*, 7 (2016), 905–917.
8. M. S. Lee, S. Sarwar, S. Park, U. Asmat, D. T. Thuy, C. H. Han, S. Ahn, I. Jeong, S. Hong, *Sustain. Energy Fuels*, 4 (2020), 3318–3325.
9. T. Wang, Z. Cheng, Y. Zhou, H. Liu, W. Shen, *J. Mater. Chem. A*, 7 (2019), 21730–21739.
10. A. Rajagopal, K. Yao, A. K. Jen, *Adv. Mater.*, 30 (2018), 1800455.
11. Q. Sun, B. Zong, X. Meng, B. Shen, X. Li, B. Kang, S. R. P. Silva, *ACS Appl. Mater. Interfaces*, 14 (2022), 6702–6713.
12. Q. Cao, Y. Li, H. Zhang, J. Yang, J. Han, T. Xu, S. Wang, Z. Wang, B. Gao, J. Zhao, X. Li, X. Ma, S. M. Zakeeruddin, W. E. I. Sha, X. Li, M. Grätzel, *Sci. Adv.*, 7 (2021).
13. X. Ding, H. Wang, Y. Miao, C. Chen, M. Zhai, C. Yang, B. Wang, Y. Tian, M. Cheng, *ACS Appl. Mater. Interfaces*, 14 (2022), 3930–3938.
14. N. H. Hemasiri, S. Kazim, L. Calio, S. Paek, M. Salado, G. Pozzi, L. Lezama, M. K. Nazeeruddin, S. Ahmad, *ACS Appl. Mater. Interfaces*, 12 (2020), 9395–9403.
15. T. Wu, R. Zhuang, R. Zhao, R. Zhao, L. Zhu, G. Liu, R. Wang, K. Zhao, Y. Hua, *ACS Energy Lett.*, 6 (2021), 2218–2228.
16. N. H. Hemasiri, S. Kazim, S. Ahmad, *J. Mater. Chem. C*, 9 (2021), 9865–9873.
17. P. You, G. Tang, J. Cao, D. Shen, T. W. Ng, Z. Hawash, N. Wang, C. K. Liu, W. Lu, Q. Tai, Y. Qi, C. S. Lee, F. Yan, *Light Sci. Appl.*, 10 (2021).
18. N. H. Hemasiri, S. Kazim, S. Ahmad, *Nano Energy*, 77 (2020) 105292.
19. B. W. N. H. Hemasiri, J. K. Kim, J. M. Lee, *Nanomicro Lett.*, 10 (2017).
20. F. Xie, G. Dong, K. Wu, Y. Li, M. Wei, S. Du, *J. Colloid Interface Sci.*, 591 (2021), 326–333.
21. P. Kumar, E. Vahidzadeh, U. K. Thakur, P. Kar, K. M. Alam, A. Goswami, N. Mahdi, K. Cui, G. M. Bernard, V. K. Michaelis, K. Shankar, *J. Am. Chem. Soc.*, 141 (2019), 5415–5436.

22. X. Yang, L. Zhao, S. Wang, J. Li, B. Chi, *J. Materiomics*, 7 (2021), 728–741.
23. L. L. Jiang, Z. K. Wang, M. Li, C. C. Zhang, Q. Q. Ye, K. H. Hu, D. Z. Lu, P. F. Fang, L. S. Liao, *Adv. Funct. Mater.*, 28 (2018), 1870047.
24. Z. Li, S. Wu, J. Zhang, Y. Yuan, Z. Wang, Z. Zhu, *Sol. RRL*, 4 (2019), 1900413.
25. D. Cruz, J. Garcia Cerrillo, B. Kumru, N. Li, J. Dario Perea, B. V. K. J. Schmidt, I. Lauermann, C. J. Brabec, M. Antonietti, *J. Am. Chem. Soc.*, 141 (2019), 12322–12328.
26. J. F. Liao, W. Q. Wu, J. X. Zhong, Y. Jiang, L. Wang, D. B. Kuang, *J. Mater. Chem. A*, 7 (2019), 9025–9033.
27. Z. Liu, S. Wu, X. Yang, Y. Zhou, J. Jin, J. Sun, L. Zhao, S. Wang, *Nanoscale Adv.*, 2 (2020), 5396–5402.
28. X. Wang, K. Maeda, A. Thomas, K. Takanabe, G. Xin, J. M. Carlsson, K. Domen, M. Antonietti, *Nat. Mater.*, 8 (2008), 76–80.
29. B. Jürgens, E. Irran, J. Senker, P. Kroll, H. Müller, W. Schnick, *J. Am. Chem. Soc.*, 125 (2003), 10288–10300.
30. J. Xu, L. Zhang, R. Shi, Y. Zhu, *J. Mater. Chem. A*, 1 (2013), 14766.
31. S. Yang, Y. Gong, J. Zhang, L. Zhan, L. Ma, Z. Fang, R. Vajtai, X. Wang, P. M. Ajayan, *Adv. Mater.*, 25 (2013), 2452–2456.
32. Y. Cui, J. Zhang, G. Zhang, J. Huang, P. Liu, M. Antonietti, X. Wang, *J. Mater. Chem.*, 21 (2011), 13032.
33. Y. Cui, Z. Ding, X. Fu, X. Wang, *Angew. Chem. Int. Ed.*, 124 (2012), 11984–11988.
34. S. Tonda, S. Kumar, S. Kandula, V. Shanker, *J. Mater. Chem. A*, 2 (2014), 6772.
35. J. Chang, Y. C. Wang, C. Song, L. Zhu, Q. Guo, J. Fang, *J. Mater. Chem. C*, 6 (2018), 6982–6987.
36. M. Liu, G. Zhong, Y. Yin, J. Miao, K. Li, C. Wang, X. Xu, C. Shen, H. Meng, *Adv. Sci.*, 4 (2017), 1700335.
37. D. J. Kubicki, D. Prochowicz, A. Hofstetter, P. Péchy, S. M. Zakeeruddin, M. Grätzel, L. Emsley, *J. Am. Chem. Soc.*, 139 (2017), 10055–10061.

38. K. Saalwächter, F. Lange, K. Matyjaszewski, C. F. Huang, R. Graf, *J Magn. Reson.*, 212 (2011), 204–215.
39. C. Blaga, G. Christmann, M. Boccard, C. Ballif, S. Nicolay, B. A. Kamino, *Sustain. Energy Fuels*, 5 (2021), 2036–2045.
40. M. T. Khan, N. H. Hemasiri, S. Kazim, S. Ahmad, *Sustain. Energy Fuels*, 5 (2021), 6352–6360.
41. N. Klipfel, J. Xia, P. Čulík, S. Orlandi, M. Cavazzini, N. Shibayama, H. Kanda, C. Igci, W. Li, Y. B. Cheng, V. Jankauskas, K. Genevicius, A. M. Asiri, C. Momblona, K. Rakstys, G. Pozzi, M. K. Nazeeruddin, *Mater. Today Energy*, 2022, 29, 101110.
42. C. Li, Z. Song, D. Zhao, C. Xiao, B. Subedi, N. Shrestha, M. M. Junda, C. Wang, C. S. Jiang, M. Al-Jassim, R. J. Ellingson, N. J. Podraza, K. Zhu, Y. Yan, *Adv. Energy Mater.*, 9 (2018), 1803135.
43. M. S. Alvar, P. W. M. Blom, G. J. A. H. Wetzelaer, *Nat. Commun.*, 2020, 11(1).
44. K. Liu, Y. Sun, Q. Li, C. Yang, M. Azam, Z. Wang, S. Qu, Z. Wang, *Nanoscale*, 11 (2019), 22467–22474.
45. Z. Luo, G. Li, W. Gao, K. Wu, Z. G. Zhang, B. Qiu, H. Bin, L. Xue, F. Liu, Y. Li, C. Yang, *J. Mater. Chem. A*, 6 (2018), 6874–6881.
46. L. Xiao, T. Liang, K. Gao, T. Lai, X. Chen, F. Liu, T. P. Russell, F. Huang, X. Peng, Y. Cao, *ACS Appl. Mater. Interfaces*, 2017, 9(35), 29917–29923.
47. H. Dhifaoui, N. H. Hemasiri, W. Aloui, A. Bouazizi, S. Kazim, S. Ahmad, *Adv. Mater. Interfaces*, 8 (2021), 2101002.
48. N. H. Hemasiri, L. Calì, M. Pegu, S. Kazim, S. Ahmad, *Sol. RRL*, (2022), 2100793.
49. J. Li, T. Jiu, C. Duan, Y. Wang, H. Zhang, H. Jian, Y. Zhao, N. Wang, C. Huang, Y. Li, *Nano Energy*, 46 (2018), 331–337.
50. C. C. Boyd, R. C. Shallcross, T. Moot, R. Kerner, L. Bertoluzzi, A. Onno, S. Kavadiya, C. Chosy, E. J. Wolf, J. Werner, J. A. Raiford, C. de. Paula, A. F. Palmstrom, Z. J. Yu, J. J. Berry, S. F. Bent, Z. C. Holman, J. M. Luther, E. L. Ratcliff, N. R. Armstrong, M. D. McGehee, *Joule*, 4 (2020), 1759–1775.
51. T. Guo, Z. Fang, Z. Zhang, Z. Deng, R. Zhao, J. Zhang, M. Shang, X. Liu, Z. Hu, Y. Zhu, L. Han, *J. Energy Chem.*, 69 (2022), 211–220.

52. S. H. Turren-Cruz, M. Saliba, M. T. Mayer, H. Juárez-Santiesteban, X. Mathew, L. Nienhaus, W. Tress, M. P. Erodici, M. J. Sher, M. G. Bawendi, M. Grätzel, A. Abate, A. Hagfeldt, J. P. Correa-Baena, *Energy Environ. Sci.*, 2018, 11(1), 78–86.
53. Y. Sun, J. Peng, Y. Chen, Y. Yao, Z. Liang, *Sci. Rep.*, 2017, 7(1).
54. Y. Cui, Z. Ding, X. Fu, X. Wang, *Angew. Chem. Int. Ed.*, 51 (2012), 11814-11818.